

AperTO - Archivio Istituzionale Open Access dell'Università di Torino

The JEM-EUSO observation in cloudy conditions

This is a pre print version of the following article:

Original Citation:

Availability:

This version is available <http://hdl.handle.net/2318/1636723> since 2017-05-19T18:41:56Z

Published version:

DOI:10.1007/s10686-014-9377-2

Terms of use:

Open Access

Anyone can freely access the full text of works made available as "Open Access". Works made available under a Creative Commons license can be used according to the terms and conditions of said license. Use of all other works requires consent of the right holder (author or publisher) if not exempted from copyright protection by the applicable law.

(Article begins on next page)

1 **JEM-EUSO observation in cloudy conditions**

2 **JEM-EUSO Collaboration**

3
4 Received: date / Accepted: date

5 **Abstract** The JEM-EUSO (Extreme Universe Space Observatory on-board the Japa-
6 nese Experiment Module) mission will conduct extensive air shower (EAS) observa-
7 tions on the International Space Station (ISS). Following the ISS orbit, JEM-EUSO
8 will experience continuous changes in the atmospheric conditions, including cloud
9 presence. The influence of clouds on space-based observation is, therefore, an im-
10 portant topic to investigate from both EAS property and cloud climatology points
11 of view. In the present work, the impact of clouds on the apparent profile of EAS
12 is demonstrated through the simulation studies, taking into account the JEM-EUSO
13 instrument and properties of the clouds. These results show a dependence on the
14 cloud-top altitude and optical depth of the cloud. The analyses of satellite measure-
15 ments on the cloud distribution indicate that more than 60% of the cases allow for
16 conventional EAS observation, and an additional $\sim 20\%$ with reduced quality. The
17 combination of the relevant factors results in an effective trigger aperture of EAS
18 observation $\sim 72\%$, compared to the one in the clear atmosphere condition.

19 **Keywords** JEM-EUSO · ultra-high energy cosmic ray · extensive air shower

20 **PACS** PACS 96.50.sd · PACS 92.60.N

Alejandro Guzmán
Institute for Astronomy and Astrophysics, Kepler Center, University of Tübingen, Sand 1, D-72076
Tübingen, Germany
E-mail: guzman@astro.uni-tuebingen.de

Guadalupe Sáez Cano
SPace and AStroparticle Group, Universidad de Alcalá, Ctra. Madrid-Barcelona km 33.7, E-28871 Alcalá
de Henares, Spain
E-mail: lupe.saez@uah.es

Kenji Shinozaki
Institute for Astronomy and Astrophysics, Kepler Center, University of Tübingen, Sand 1, D-72076
Tübingen, Germany
Tel.: +49-7071-29 25279
Fax: +49-7071-29 3458
E-mail: shinozaki@astro.uni-tuebingen.de

1 Introduction

The space-based extensive air shower (EAS) observation, as employed in the JEM-EUSO (Extreme Universe Space Observatory on-board the Japanese Experiment Module) mission [1–5], is a novel approach for investigating ultra-high energy cosmic rays (UHECRs; referred to as $\gtrsim 5 \times 10^{19}$ eV). The fluorescence technique is applied to search for the moving track of ultra-violet (UV) photons produced in EAS development in the nighttime atmosphere. This technique has been established by the ground-based experiments [6] but has never been put into practice in space, thus requiring specific considerations. In the present article, we discuss characteristics of EAS observed in different atmospheric conditions by the JEM-EUSO mission, focusing on the role of clouds.

The JEM-EUSO observatory is an ensemble of the UV telescope, referred to as ‘main telescope’, the atmospheric monitoring (AM) system [7, 8], and other subsystem instruments. It is designed to operate on the JEM *Kibo* module of the International Space Station (ISS) [9, 10]. Orbiting at a nominal altitude $H_0 \sim 400$ km from the Earth’s surface¹, it revolves every ~ 90 min at a speed of ~ 7.6 km s⁻¹. On average, the ISS spends $\sim 34\%$ of the time in umbra of the Earth, during which the EAS observation may be conducted. Accounting for the effect due to back-scattered moonlight, the EAS observation duty cycle is expected to be $\sim 20\%$ [11]. According to the inclination, the ISS operation ranges between the latitudes $\pm 51.6^\circ$.

The main telescope is designed to have a wide field-of-view (FOV), covering an area of $\sim 1.4 \times 10^5$ km² in nadir observation. It consists of a 4.5-m² refractive optics and a focal surface (FS) detector. The FS detector is formed by 137 photo-detector modules (PDMs) [4, 12]. Each PDM is a set of 36 multi-anode photomultiplier tubes (MAPMTs) having 64 pixels with a spatial window of 0.075° equivalent to ~ 0.5 km on the Earth’s surface. The integration time of data acquisition is 2.5 μ s and is called gate time unit (GTU). Two levels of trigger algorithms [13] search every PDM for stationary and transient excesses of EAS signals against prevailing background light.

The AM system consists of an infra-red (IR) camera [14, 15] and a steerable UV laser system [7, 8]. To characterize the cloud distribution, the IR camera measures the brightness temperature distribution over the FOV of the main telescope. This provides the relative distribution of the cloud-top altitude in the FOV. The laser system with the main telescope acting as a receiver allows a LIDAR (light detection and ranging) technique to sound the atmospheric properties along the line of sight of interest. LIDAR information is used to calibrate the brightness temperatures with the absolute altitude. Clouds with small optical depths may be observed with temperatures that do not correspond to the actual altitudes. In this case, LIDAR information that aims to distinguish between clear atmosphere and clouds with given thresholds in optical depth may label the EAS events taking place in such regions. For details regarding instrument, operation, data treatment, etc. of the AM system, see Ref. [7, 8, 16, 17].

In the following sections, we estimate the efficiency of the EAS observation in atmospheric conditions, with and without clouds, using dedicated simulation studies

¹ Hereafter, Earth’s surface is referred to as the assumed Earth’s ellipsoid model and the altitude is measured from this level.

63 for the JEM-EUSO mission. We also analyze the cloud coverage using available
64 databases from meteorological missions. Combining both factors, we estimate the
65 overall observation efficiency with a perspective towards event reconstruction.

66 **2 EAS observable properties and efficiency of trigger under cloudy conditions**

67 In UHECR observation by optical means, isotropically emitted fluorescence light is
68 the dominant component of the signals and its luminosity is almost proportional to
69 the energy deposited by the EAS particles. Highly beamed Cherenkov light is also
70 produced close to the particle trajectory. A part of this light may reach the JEM-
71 EUSO telescope once it is scattered in the atmosphere towards the direction of the
72 telescope. In addition, the space-based observation also detects the diffusely reflected
73 Cherenkov photons from land or water. A similar effect takes place at the impact
74 of photons on cloud. Those reflected signals, referred to as ‘Cherenkov footprint’,
75 provide a piece of information on the position and timing of the EAS reaching such
76 boundaries. The geometrical configuration constrains uncertainty in distance to the
77 EAS, as well. In general, space-based fluorescence observation favors EASs from
78 large zenith angles with little effect of aerosols near the Earth’s surface. These points
79 simplify full calorimetric measurement of the development of EAS.

80 In actual observation, ground-based observatories are affected by local weather
81 conditions. As far as the influence of clouds is concerned, the EAS observation can be
82 performed without further consideration by selecting times without cloud coverage.
83 In this case, the exposure is only lowered by the reduction of observation time. On
84 the other hand, space-based telescopes overlook continuously changing landscapes
85 within their wide FOV. The atmospheric conditions are also largely variable by lo-
86 cation and time along the satellite trajectory. This leads the JEM-EUSO telescope to
87 watch all possible conditions, in particular presence of clouds in the FOV. The time-
88 scale of transitions between cloudy and clear atmosphere conditions may be an order
89 of minute or shorter. Seasonal variations also appear every ~ 20 min, namely quar-
90 ter of the orbital period. However, the presence of clouds is only relevant if the EAS
91 takes place behind the cloud, especially those with large optical depths. The influence
92 of the cloud is obviously dependent on their top altitude. Therefore, the portion of
93 FOV where high-altitude clouds exist may reduce the instantaneous aperture of EAS
94 observation, while it is possible to detect EAS events within the remaining portion.

95 The observed temporal and topological profiles of the signals are used to retrieve
96 the geometry and longitudinal development of the EAS (see Refs. [18–20] for details
97 about technique and performances). In practice, the so-called shower-detector-plane
98 (SDP), the plane containing the EAS track and the detector, is determined by orienta-
99 tion of the signals projected on the FS detector. The apparent angular velocity of the
100 light spot indicates the incident direction of the EAS within SDP, presuming that it
101 moves with the EAS at the speed of light. Cherenkov footprint or other methods [3,
102 19] can be used to determine the distance to the EAS. Knowing the EAS geome-
103 try and taking into account extinction loss, the arrival time distribution of photons,
104 namely light curve, may be converted to the energy deposition profile along the EAS.
105 Photons from EAS, heading towards the JEM-EUSO telescope, pass on or near SDP.

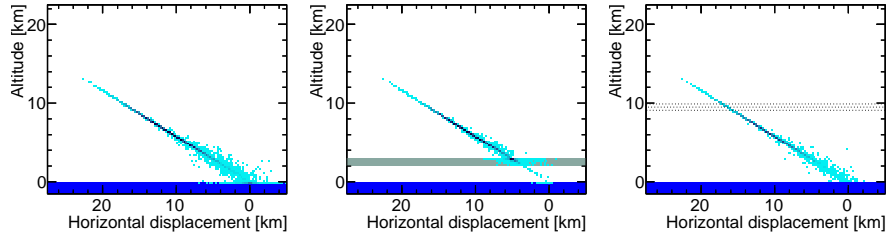


Fig. 1 Schematic view of EAS geometry for $\Theta = 60^\circ$ in the different atmospheric conditions. The left panel shows the observed photon distribution projected on SDP for the clear atmosphere condition. The middle and right panels are same but for the cloudy cases of large optical depth at 3 km and of small optical depth at 10 km, respectively.

106 If a cloud is located between EAS and the detector on that plane, the apparent profile
 107 of the signals is affected.

108 In Fig. 1, a schematic view of EAS geometry is illustrated in the different atmos-
 109 pheric conditions. The left panel shows the observed photon distribution projected on
 110 SDP for the clear atmosphere condition. The middle and right panels are the same
 111 except for the cloudy cases of large optical depth at 3 km, and of small optical depth
 112 at 10 km, respectively. In this example, the zenith angle Θ of the EAS is 60° .

113 In the clear atmosphere condition, provided that a bright enough portion of the
 114 EAS is contained within the wide-FOV, our space-based telescope is capable of
 115 detecting said EAS. Moreover, in many of the cases this entire portion of EAS can be
 116 followed until its impact on the Earth's surface.

117 In order to investigate such effects, we employ ESAF (EUSO Simulation and
 118 Analysis Framework) [21]. In the ESAF version used in the present work, the JEM-
 119 EUSO configuration is implemented [11]. The primary UHECR is assumed to be
 120 protons. In addition to the clear atmosphere condition, we simulate EASs through a
 121 homogeneous-layer test cloud, with a given cloud-top altitude H_C and optical depth
 122 τ_C . Unless otherwise noted, τ_C hereafter means the vertical optical depth of the cloud
 123 components. In the setup of ESAF, two models of the phase function for photon scatter-
 124 ing, namely cumulus- [22] and cirrostratus- [23] models, are available to simulate
 125 this process. In practice, these models represent the cases for clouds formed by water
 126 droplets and ice crystals depending on altitude, respectively. As the scope of the
 127 present article is the impact of the cloud on the trigger exposure, the photon intensity
 128 at the telescope pupil is more relevant. In this sense, the optical depth is the key
 129 parameter for determining such value. In our simulation, the former model is chosen,
 130 however, and the effective difference between these models is only apparent in small
 131 scattering angles within $\sim 10^\circ$. Such difference may be important in the case that,
 132 unlikely for spaced-based observation, the telescope may see the direct Cherenkov
 133 photons.

134 In Fig. 2, the top panel shows the light curves of a typical EAS in different atmos-
 135 pheric conditions. The sample is the case for the EAS of $E = 10^{20}$ eV from $\Theta = 60^\circ$.
 136 The solid line represents the case for the clear atmosphere. Dashed and dotted lines
 137 denote the cases for clouds of $\tau_C = 1$ at $H_C = 3$ km and of $\tau_C = 0.5$ at $H_C = 10$ km,

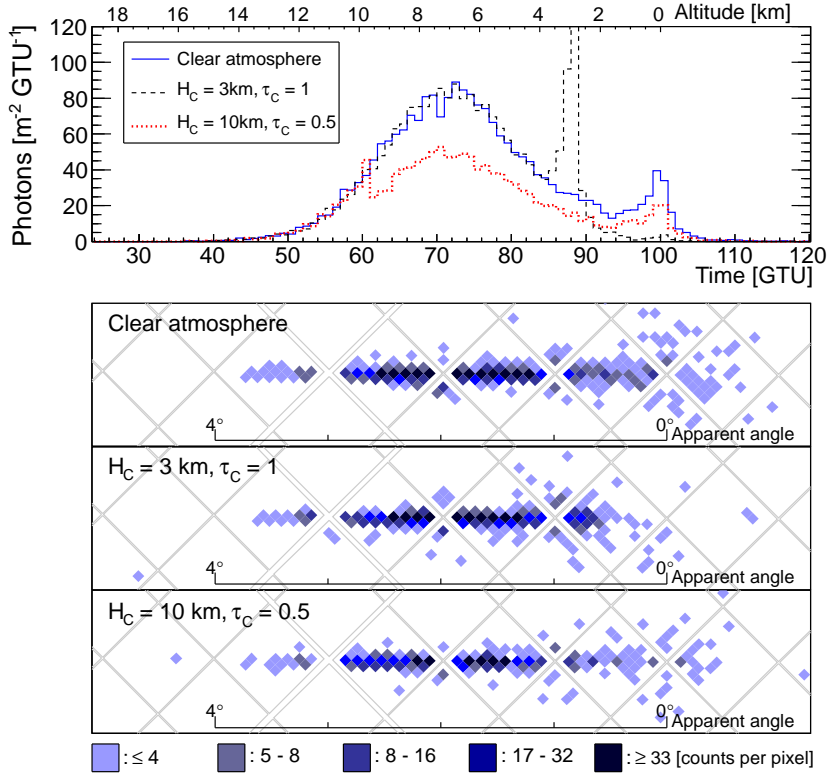


Fig. 2 Arrival time distribution of photons (top panel) from a proton induced EAS of $E_0 = 10^{20}$ eV and $\Theta = 60^\circ$ for different atmospheric conditions. The solid line represents the case for the clear atmosphere. Dashed and dotted lines denote the cloudy cases for $\tau_C = 1$ at $H_C = 3$ km and $\tau_C = 0.5$ at $H_C = 10$ km, respectively. The axis on the top indicates the altitude where photons originate for the given arrival time. Bottom panels show the time-integrated images of signals on the FS detector for those three cases. The color scale indicates the number of signal counts per pixel. The horizontal position along the axis corresponds to the arrival time shown on the top panel. The gray lines indicate the boundaries of MAPMTs.

138 respectively. The horizontal axis is the absolute time. The time that the first shower
 139 particles reach the Earth's surface is set at 100 GTUs. The axis on the top indicates
 140 the altitude where photons originate for the given arrival time. Bottom panels display
 141 the time-integrated images of signals on the FS detector for those cases. The color
 142 scale indicates the number of signal counts per pixel. The horizontal position along
 143 the axis corresponds to the arrival time shown on the top panel.

144 In the clear atmosphere condition, the light curve indicates the EAS development,
 145 followed by the Cherenkov footprint on the surface. For EASs from $\Theta = 60^\circ$ in this
 146 example, the apparent movement extends $\sim 2.5^\circ$ and lasts ~ 50 GTUs ($=125 \mu\text{s}$).
 147 Using these observable data, the EAS parameters are reconstructed.

148 In case of the presence of clouds, EAS signals that appear are modified. If the
 149 optical depth of the cloud is large enough, the apparent shower track is effectively
 150 truncated. Upward photons scattered or emitted below the cloud are extinguished and

Table 1 Average $\zeta(E)$ for different test clouds for $E > 6.3 \times 10^{19}$ eV with an assumed flux of $\propto E^{-3}$ [11].

Cloud-top altitude H_C	Optical depth τ_C			
	0.05	0.5	1.5	5
10 km	88%	66%	37%	18%
7.5 km	89%	69%	43%	26%
5 km	88%	82%	74%	70%
2.5 km	90%	89%	89%	90%

do not contribute to the signals at the telescope. In this example, with a cloud at 3 km, the apparent signals extend $\sim 2.5^\circ$ and last 40 GTUs. It is still feasible to apply the reconstruction techniques used in the case of the clear atmosphere by only using the measurements taken above the cloud.

As seen in the figure for the case of a small optical depth, photon signals that originated below the cloud are attenuated. This lowers the estimated energy of the EAS if the same techniques for the clear atmosphere are applied. Alternatively, the Cherenkov footprint is still observable and the orientation and apparent angular velocity are not affected, thus, the repercussion on arrival direction determination is limited.

To estimate the efficiency for EAS observation in cloudy conditions, we first define the ‘geometrical aperture’ that represents trigger aperture, assuming a single homogeneous atmosphere condition over the observation area. In practice, the geometrical aperture is determined by a number of EASs simulated over an area S_{sim} far larger than that effectively observable by the telescope. For N_{trig} triggering samples among N_{sim} simulated EASs, the geometrical aperture is defined as follows:

$$A \equiv \frac{N_{\text{trig}}}{N_{\text{sim}}} \cdot S_{\text{sim}} \cdot \Omega_0, \quad (1)$$

where $\Omega_0 = \pi$ [sr] is the solid angle acceptance for $0^\circ \leq \Theta \leq 90^\circ$. In clear atmosphere condition, it reaches $\sim 4.4 \times 10^5 \text{ km}^2 \text{ sr}$ at $\sim 10^{21}$ eV [11]. Then we define ζ as the ratio of geometrical aperture in cloudy conditions to that in the clear atmosphere condition. It is expressed as a function of energy by

$$\zeta(E; H_C, \tau_C) = \frac{A(E; H_C, \tau_C)}{A_0(E)} \quad (2)$$

where $A(E; H_C, \tau_C)$ and $A_0(E)$ are geometrical apertures as a function of energy for the case with the test cloud and for clear atmosphere condition, respectively.

Table 1 summarizes the average ζ above 6.3×10^{19} eV for different test clouds [11]. The differential flux of EASs is assumed to be $\propto E^{-3}$.

For clouds at higher altitudes, the cases with large optical depths indicate significant suppression in the geometrical aperture. This is explained by a reduction of the photon flux at the main telescope.

In the case of clouds at lower altitudes, only a small portion of photons are affected. For $\Theta \gtrsim 25^\circ$, the maximum of the EAS development takes place above ~ 3 km altitude. This particularly means that the case of the low-altitude cloud can be regarded as practically clear atmosphere for EASs from larger zenith angles.

182 For clouds with optical depths such as $\tau_C = 0.05$, the reduction of signals is almost
 183 independent of cloud-top altitudes and its influence for trigger algorithms is negligi-
 184 bly small. In the case of clouds with $\tau_C = 0.5$, the signal reduction produced by the
 185 cloud is slightly dependent on the altitude. Naturally, the higher the cloud is, the more
 186 EAS light is absorbed, however, for trigger algorithms its influence is limited.

187 3 Climatological average of cloud distribution

188 In the following, we analyze existing satellite measurements from CALIPSO (Cloud
 189 Aerosol Lidar and Infrared Pathfinder Satellite Observations) [24] and compare them
 190 with the measurements from TOVS (TIROS Operational Vertical Sounder) [25]. As
 191 described in the previous section, the degree of cloud influence on the EAS observation
 192 depends greatly on the properties of clouds. It is, therefore, important to evaluate the
 193 cloud distribution over the geographical regions covered by the ISS orbit.

194 The NASA project TOVS, on-board NOAA's TIROS series of polar orbiting
 195 satellites, consists of three instruments: High-Resolution IR Sounder Modification 2;
 196 Stratospheric Sounding Unit; and Microwave Sounding Unit. These instruments had
 197 been designed to determine the radiance that is needed to calculate temperature and
 198 humidity profiles up to the stratosphere. These data have a good spectral distribution
 199 and provide the optical depth and altitude of clouds, applying their own radiative
 200 transport model. In the present work, we use data taken between 1988 and 1994.

201 CALIPSO forms a part of the A-Train Satellite Constellation [26], a group of
 202 satellites which carry out atmospheric measurements. CALIPSO consists of a two-
 203 wavelength polarization-sensitive LIDAR, and two passive imagers operating in the
 204 visible and IR bands. Data from these instruments are used to determine the verti-
 205 cal distribution of clouds and aerosols, along with their optical and physical prop-
 206 erties. CALIPSO performs a sun-synchronous orbit at an altitude of 705 km with a
 207 98.2° inclination. With a 60-m vertical resolution measurement by CALIOP (Cloud-
 208 Aerosol Lidar with Orthogonal Polarization) [27], CALIPSO's LIDAR, the extinc-
 209 tion coefficients of the clouds $\alpha_C(h)$ are provided as a function of altitude up to
 210 20.2 km. The horizontal resolution is 5 km along the orbit. Cloud data from CALIOP
 211 are incorporated into the Imaging Infra-red Radiometer (IIR) retrieval algorithm [28].

212 To compare with the analysis of the TOVS data, the cloud optical depth τ_C is
 213 determined by integrating $\alpha_C(h)$ from 20.2-km altitude to the surface boundary,
 214 namely either water or land. Since the LIDAR measurement can penetrate through
 215 the clouds, there is no unique definition for cloud top in the CALIPSO data. There-
 216 fore, for the CALIPSO analysis, we define the cloud-top altitude H_C as the altitude
 217 below which the optical depth exceeds 0.1, namely

$$\int_{H_C}^{20.2 \text{ [km]}} \alpha_C(h) dh = 0.1. \quad (3)$$

218 If $\tau_C < 0.1$, no cloud-top altitude is determined and the region under the scope is
 219 counted as clear atmosphere.

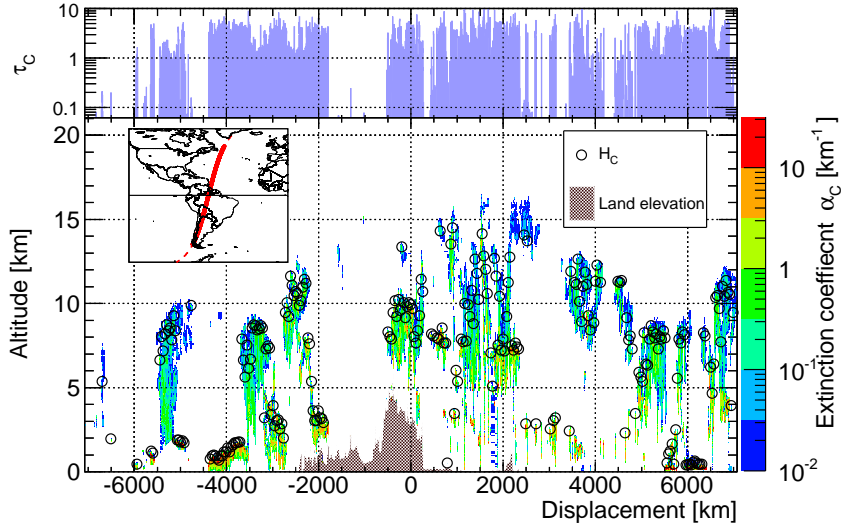


Fig. 3 An example of CALIPSO data for the α_C profile in color scale on the coordinates of altitude versus elongated displacement along the orbit shown in the lower part. The shaded region represents the land elevation. H_C are indicated at every 50-km displacement by circles. τ_C are indicated in the upper part. The data were taken on May 1st, 2010, along a part of the orbit within $\pm 51.6^\circ$ latitudes shown by the bold curve on the inset map. The origin of the horizontal axis is at the Equator and positive values represents the North Hemisphere.

220 Fig. 3 demonstrates an example of the α_C profile in color scale from CALIPSO.
 221 In the lower part of the figure, the coordinates are altitude versus northward displace-
 222 ment from the Equator along the orbit. H_C is also indicated at every 50-km displace-
 223 ment by circles. The land elevation is represented by the shaded region. In the upper
 224 part, τ_C is indicated by the histogram. The data were taken on May 1st, 2010 and are
 225 limited to within $\pm 51.6^\circ$ latitudes along the part of the orbit shown in the inset map.

226 In this example, one can see clouds in various regions with widely distributed
 227 cloud-top altitudes below ~ 15 km. Clear atmosphere regions are also observed around
 228 -1500 -km- and -6000 -km- displacements and several other places. There are also
 229 regions with relatively low cloud-top altitudes, for example around -4000 -km dis-
 230 placement, where only the observation of near-vertical EASs are affected.

231 In the present work, we use a sample of the CALIPSO database selected over the
 232 year 2010, and apply the above calculations. By analyzing the databases mentioned
 233 above, the probability distribution functions $\mathcal{F}_C(H_C, \tau_C)$ that give the relative occur-
 234 rence of the cloud types are obtained. The climatological average of the clouds is
 235 inferred from these functions. To characterize the cloud, we first categorize clouds by
 236 their top altitudes H_C into four ranges of < 3.2 km, $3.2 - 6.5$ km, $6.5 - 10$ km and
 237 > 10 km. In addition, the optical depths τ_C are tabulated into four ranges of < 0.1 ,
 238 $0.1 - 1$, $1 - 2$ and > 2 . In both databases, we only select the entries of nighttime
 239 measurements in the region within $\pm 51.6^\circ$ latitudes.

Table 2 Relative occurrence of cloud categories over the ISS orbit, taken from the TOVS and CALIPSO presented as a matrix of cloud-top altitude versus optical depth. For CALIPSO analysis, the cases with $\tau_C < 0.1$ are all summed up as clear atmosphere. The analysis of TOVS is from Ref. [11].

Cloud-top altitude H_C	Relative occurrence (TOVS)				Relative occurrence (CALIPSO)			
	Optical depth τ_C							
	<0.1	0.1–1	1–2	> 2	<0.1	0.1–1	1–2	> 2
> 10 km	1.2%	5.0%	2.5%	5.0%		4.7%	4.7%	4.7%
6.5–10 km	< 0.1%	3.2%	4.2%	8.5%	38%	4.5%	4.8%	6.0%
3.2–6.5 km	< 0.1%	2.0%	3.0%	6.0%		3.2%	1.7%	6.4%
< 3.2 km	31%	6.4%	6.0%	16%		2.8%	0.9%	17%

Table 3 Comparison of clouds occurrence results from TOVS and CALIPSO data. Types of cloudy conditions are assumed: (a) for low-cloud or $\tau_C < 0.1$, (c) for high-cloud with $\tau_C > 1$ and (b) for any other intermediate.

Cloud-top altitude	Relative occurrence (TOVS)				Relative occurrence (CALIPSO)		
	Optical depth τ_C						
	< 0.1	0.1–1	> 1	Type	> 1	0.1–1	< 0.1
HC ($H_C > 6.5$ km)			20%	(c)	20%		
MC ($H_C = 3.2 - 6.5$ km)		19%		(b)		21%	
LC ($H_C < 3.2$ km)	61%			(a)			59%

240 In Table 2, the relative occurrence of cloud properties from analyses of TOVS and
 241 CALIPSO data are summarized on an H_C - τ_C matrix. As mentioned above, the clouds
 242 with $\tau_C < 0.1$ for CALIPSO are classified as clear atmosphere.

243 In Table 3, results from TOVS and CALIPSO data are compared. Following the
 244 meteorological convention [29], clouds are sorted by their top altitudes into low-
 245 cloud (LC; $H_C < 3.2$ km), middle-cloud (MC; $H_C = 3.2 - 6.5$ km), or high-cloud
 246 (HC; $H_C > 6.5$ km). In addition to optical depth, they are summarized by types (a),
 247 (b), and (c) as defined below. Dividing matrices in Table 2, we use three types: (a) for
 248 LC or $\tau_C < 0.1$, (c) for HC with $\tau_C > 1$ and (b) for other cases. The type (b) includes
 249 MC with $\tau_C > 0.1$ and, otherwise, ones with $\tau_C = 0.1 - 1$, excluding the LC cases.

250 First of all, the results from the two analyses are in good agreement. The influ-
 251 ence of clouds at higher altitudes and/or with larger optical depths is more significant
 252 to the EAS observation. ‘Optically thick’ high-clouds may especially reduce the effi-
 253 ciency of EAS observation, as can also be seen in Table 1. This corresponds to type
 254 (c). Note that this effect does not apply to the EAS from large zenith angles. For the
 255 intermediate type (b), the detection of such clouds is relevant so that EASs detected
 256 under such conditions are not confused with those under the type (a). On the other
 257 hand, in the type (a) case, low-clouds for most of the EASs may act as a clear at-
 258 mosphere that do not hide the brightest part of EAS development. In this case, the
 259 cloud-top altitude within FOV of the main telescope is determined by the IR camera
 260 measurement to discriminate the cloud-free interval of light curves as seen in Fig. 2.

261 Apart from the average occurrence of clouds, the global distribution and seasonal
 262 dependence are also relevant in space-based observation. They result from a complex
 263 system of geographical, eg. land versus ocean, meteorological, and other factors (see
 264 Ref. [11, 29] for discussion). We investigate the TOVS database, covering a period of
 265 7 years, in all possible locations for JEM-EUSO. The nighttime duration is 34% on

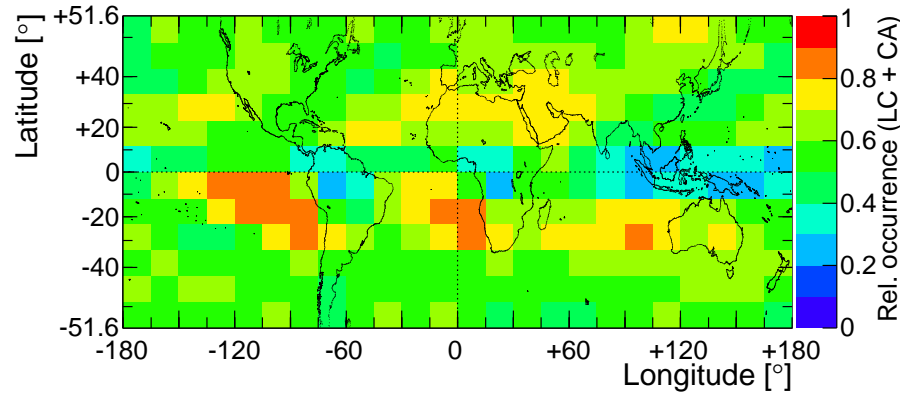


Fig. 4 Global distribution of occurrence of the sum of low-cloud and clear atmosphere from TOVS data in color scale. The projection reproduces a constant residence time of the ISS in each bin.

Table 4 Average relative occurrence of different cloud types by three-month seasons of year. The sum of types (a) plus (b), and the case of type (a) alone are summarized for each Earth's hemisphere.

Type	Hemisphere	Month of year (March, April, . . . , February)											
		M	A	M	J	J	A	S	O	N	D	J	F
(a)+(b)	North	81%			76%			79%			82%		
	South		79%			83%			82%			72%	
(a)	North	59%			56%			59%			60%		
	South		60%			65%			64%			58%	

266 average over the ISS orbit, largely depending on latitudes due to the different twilight
 267 durations. To reduce such uncertainties, all data, including daytime, are analyzed.

268 Fig. 4 indicates the global map of the occurrence of low-cloud (LC) plus clear
 269 atmosphere (CA) in color scale, averaging all the data. The projection of the map
 270 reproduces a constant residence time of the ISS in each bin.

271 As previously mentioned, such conditions do not or only slightly affect the appar-
 272 ent signals of EASs. Therefore, a high occurrence of these conditions is advantageous
 273 for EAS observations. In addition to the argument in Table 3, the global average is
 274 61% for the occurrence of favorable conditions. It is worthwhile to mention that there
 275 are regions with distinctly low and high occurrences. The former regions are found in
 276 land around equatorial zones that coincide with tropical rainforest climate in Köppen
 277 classification [30]. The latter widely appear above oceans, especially in the South
 278 Hemisphere. Relatively high occurrences of favorable condition are also seen in the
 279 regions of desert climate in North Africa, Middle East, and Australia.

280 Table 4 shows the average relative occurrence of different cloud types as a func-
 281 tion of season of year. The sum of types (a) plus (b), and the case of type (a) alone
 282 are summarized as three-month average for each Earth's hemisphere.

283 In general, the seasonal variation in every test case is a small effect with an
 284 order of $\pm 5\%$ of the average. The difference in the average between hemispheres
 285 is marginal, while in both hemispheres, winter tends to have higher occurrence than

286 summer. The altitude where clouds are formed depends on temperature. The fiducial
 287 volume for EAS observation thus increases in the winter as the cloud-top altitudes
 288 descend. Note that the data used in this analysis also contain the daytime measure-
 289 ments. For the daytime, the cloud coverage is similar to that for nighttime [11,29].
 290 Note that the temperatures are higher and hence cloud altitudes are also higher. The
 291 result herein thus constitutes a conservative estimation of the occurrence of favorable
 292 condition for EAS observations from space.

293 4 Overall efficiency of EAS observation

294 The overall exposure in the JEM-EUSO mission obviously suffers from the presence
 295 of clouds. Such an impact is estimated as a ratio for the average effective aperture to
 296 the geometrical aperture for clear atmosphere. This is expressed as the convolution of
 297 the trigger efficiency and the occurrence of assumed cloud properties in the present
 298 work. Using the already defined function ζ weighted by \mathcal{F} , the average ratio κ'_C in
 299 aperture to that in clear atmosphere $A_0(E)$ is written as follows:

$$\kappa'_C(E) = \int_0^{H_0} \int_0^\infty \zeta(E; H_C, \tau_C) \cdot \mathcal{F}(H_C, \tau_C) d\tau_C dH_C. \quad (4)$$

300 After the EASs have triggered the detector, the reconstruction of these events
 301 follows. To achieve reasonable accuracies, we impose a minimal requirement: the
 302 visibility of the EAS maximum. We require that the EAS reaches its maximum above
 303 the cloud-top altitude or when the cloud has $\tau_C < 1$. The latter case includes clouds
 304 of the type (b) in our classification. In such situations, estimations of energy and
 305 determination of maximum position suffer from the distorted light curve. Therefore,
 306 the observed EAS events should be carefully treated. There may be cases that requires
 307 these events to be eliminated in scientific analysis. However, in addition to the type
 308 (a) case, these events can still be used for analysis of arrival direction that does not
 309 need the highest quality of EAS data. In both cases, enough information from signals
 310 above and through the cloud is obtained since the arrival direction determination is
 311 simply based on unchanged apparent angular velocity of EASs.

312 Taking this requirement into account, Eq. (4) is revised as follows:

$$\kappa_C(E) = \frac{1}{A_0(E)} \cdot \int_0^{H_0} \left[\int_1^\infty A(E, H_C, \tau_C | H_C < H_{\max}) \cdot \mathcal{F}(H_C, \tau_C) d\tau_C \right. \\ \left. + \int_0^1 A(E, H_C, \tau_C) \cdot \mathcal{F}(H_C, \tau_C) d\tau_C \right] dH_C \quad (5)$$

313 where H_{\max} is the altitude of the EAS development maximum. In the present analysis,
 314 TOVS data is used to estimate $\mathcal{F}(H_C, \tau_C)$.

315 In Fig. 5, the relation between κ'_C and energy is shown by triangles and κ_C is
 316 plotted by closed circles [11]. The error bar denotes an estimated uncertainty on the
 317 points, mainly due to the cloud coverage data.

318 Including cloudy condition, κ'_C is 80% or higher at energies of interest. It increases
 319 with energy. Around 10^{21} eV, the trigger aperture is nearly the same as that in clear

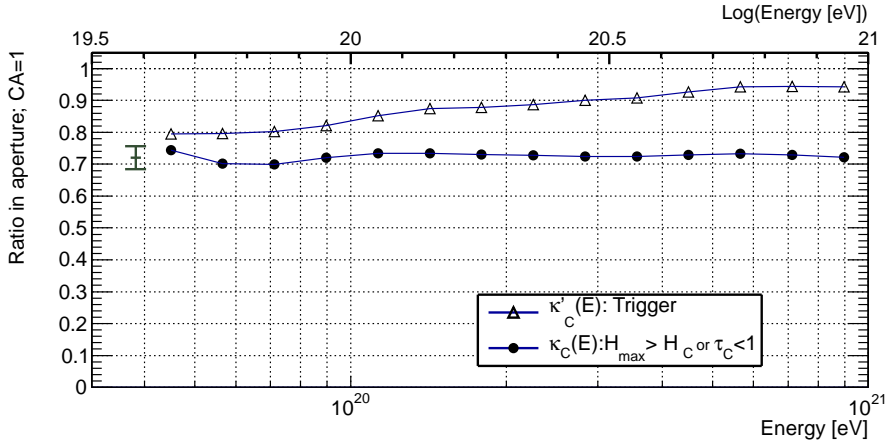


Fig. 5 Ratio of the geometrical aperture for averaged cloudy condition to that from clear atmosphere as a function of energy [11]. The triangles and circles show κ'_c and κ_c defined in Eqs. (4) and (5), respectively. In the latter case, $H_c < H_{\max}$ or $\tau_c < 1$ are required for triggering EAS events. The error bar denotes an estimated uncertainty on κ_c .

320 atmosphere. At such energies, a large number of photons still reaches the telescope
 321 to trigger it despite the extinction loss in the cloud. The reference aperture $A_0(E)$ for
 322 clear atmosphere condition can be found in Ref. [11, 31].

323 If the criterion of visibility of the EAS maximum is applied, the corresponding
 324 efficiency κ_c is almost constant $\sim 72\%$. The independence of energy is limited due
 325 to the fact that X_{\max} , the atmospheric depth at EAS maximum, does not vary much
 326 within the concerned energy range [32], while H_{\max} increases with zenith angles. For
 327 EASs from proton with $E = 10^{20}$ eV, H_{\max} is ~ 3 km, ~ 7 km and ~ 11 km for $\Theta =$
 328 30° , 60° and 75° , respectively. In most zenith angles, it is higher than typical cloud-
 329 top altitudes during nighttime as seen in Tables 2 and 3. This criterion ensures that the
 330 apparent EAS profile does not introduce significant distortion to fitting of the EAS
 331 profile. It is worthwhile to mention that our results seem dependent on combinations
 332 of hadronic interaction models and primary particles. However, κ' only varies by
 333 $\sim \pm 4\%$, changing H_{\max} by 1 km for the TOVS data. Note that 1-km difference in
 334 altitude is equivalent to typical X_{\max} dependence among those combinations.

335 In Ref. [11, 31], $\kappa_c(E)$ is referred to as the ‘cloud efficiency’. It is an impor-
 336 tant factor for estimating the effective exposure of the JEM-EUSO mission. De-
 337 tailed studies about the reconstruction in clear atmosphere condition are described
 338 in Refs. [18–20]. It should be emphasized that the information retrieved by the AM
 339 system may be of use to eliminate the low quality region in FOV based on local cloud
 340 properties [8, 15]. Further study on reconstruction in cloudy conditions is in progress.

341 5 Summary and discussion

342 In the present article, we give an overview of the EAS observation technique in cloudy
343 conditions for the JEM-EUSO mission. We focus on the following aspects: the influ-
344 ence of cloud presence on space-based EAS observation; the distribution of the clouds
345 sorted with their properties, as well as, geographical and seasonal dependence; and
346 the estimation of the overall observation efficiency.

347 For the space-based observation, the influence of the clouds varies with cloud-top
348 altitude and optical depth. It also depends on the zenith angle of the EAS, relating to
349 the altitude of development. From EAS simulation studies with commonly accepted
350 interaction models [32], the difference of X_{\max} at $E = 10^{20}$ eV is $\sim 100 \text{ g cm}^{-2}$
351 between proton and iron induced EASs. This means that the latter reach maximum
352 development at ~ 1 -km higher than the former. The influence of cloud presence is
353 weaker for this case. Thus, the simulation studies with proton primaries, therefore,
354 constitutes a conservative performance estimation.

355 Low-clouds only affect the final stage of EAS development. The light curve still
356 allows energy and X_{\max} to be reconstructed since the relevant part of the development
357 is observable without distortion. The arrival direction of UHECRs is determined by
358 means of the same approach used for clear atmosphere condition, as well. For low
359 clouds with substantial optical depth, the AM system will locate them, along with
360 their top altitude distribution [8, 15]. Utilizing these additional pieces of information,
361 the Cherenkov footprint gives far better determination on the impact position on the
362 cloud. Though it is not studied in detail, we wish to mention that such clouds lo-
363 cated in mildly light-polluted urban areas may play a positive role in blocking the
364 anthropogenic light and, therefore, allowing for EAS measurement, as well.

365 High-clouds, with relatively small optical depths, only slightly attenuate the pho-
366 tons from the EAS. In this case, the information on the EAS tracks with its temporal
367 development is obtained with little or no disturbance. This allows for the EAS events
368 obtained in such condition to be used for arrival direction distribution analysis. The
369 estimated energy is potentially affected, seen as if the EAS is of a lower energy. For
370 those atmospheric conditions, the importance of atmospheric monitoring is more pro-
371 nounced. To tag these kinds of events, the region in the FOV with such an atmospheric
372 condition are identified in the AM system within its sensitivity [8].

373 The overall influence of the clouds is more dependent on their climatological
374 properties. The analyses of TOVS and CALIPSO databases show consistent distri-
375 butions of clouds sorted by the expected degrees of influence to EAS observation.
376 The average cloud properties from the TOVS database studied in Ref. [11], is found
377 to be in good agreement with the result from the CALIPSO database. Referring to
378 the TOVS result, the occurrence of clear atmosphere is 32%. One can assume that
379 this case guarantees good condition for both ground-based and spaced-based ob-
380 servations. Moreover, for the space-based observation, the cumulative occurrence
381 increases up to 61% by adding the low-cloud cases. On these conditions, the ob-
382 served events may be used for arrival direction, spectrum and X_{\max} analyses, meet-
383 ing observational requirements of the mission [2]. Another 20% case of the cloudy
384 condition still allows a significant fraction of signals from the EAS to reach the JEM-
385 EUSO telescope. Using information of the AM system, triggered events observed un-

386 der such circumstances are clearly labeled to discriminate from those with the above
387 mentioned good condition.

388 In this case for each observed EAS event, arrival direction is only little affected,
389 despite the uncertainty by the extinction loss in the cloud with weakly constrained
390 optical depth. On the other hand, a likely distorted light curve prevents precise deter-
391 mination of energy and X_{\max} . By determining the lower bound of the primary energy
392 estimated by the amount of signals from EAS, these events may be used for scientific
393 analysis that does not require the best quality of the data.

394 In the present work, we evaluate the global distribution with TOVS. The result
395 shows some locality that is explained by conventional knowledge on the climate.
396 The annual variation is only found at an order of a few percent. We also note that
397 the annual variation acts as a factor in exposure distribution on Celestial Sphere [11,
398 31]. As a convolution of the cloud population and the observation efficiency, the
399 aperture at energies of interest is 80% and higher in comparison with that in the clear
400 atmosphere condition. Taking into account the visibility of the EAS maximum, the
401 overall cloud efficiency κ_C is evaluated to be 72 %. This factor is one of the key
402 parameters in expected exposure evaluation (see Ref. [11,31]).

403 It should be mentioned that simulation studies in Refs [3,33] showed the feasibil-
404 ity of reconstructing EAS with reasonable accuracy in the presence of clouds. For a
405 given energy, the apparent length of EAS signals mainly depends on the zenith angle.
406 The quality of reconstruction for events truncated by a cloud may be comparable to
407 the case with a smaller zenith angle in clear atmosphere (see Refs. [18–20]). In ad-
408 dition to the data measured from the AM system [8, 15], meteorological information
409 from ground stations satellites, and global models are also available for the FOV of
410 the JEM-EUSO telescope at any given time. Further studies are in progress towards
411 the development of a data analysis scheme, including all available information from
412 the main telescope, the AM system and other data regarding atmospheric conditions.

413 Acknowledgments

414 The present work has been supported in part by the European Space Agency Top-
415 ical Team activities; for German consortium by Deutsches Zentrum für Luft- und
416 Raumfahrt; the Helmholtz Alliance for Astroparticle Physics funded by the Initiative
417 and Networking Fund of the Helmholtz Association, and for Spanish consortium by
418 Ministerio de Ciencia e Innovación under projects AYA2009-06037-E/ESP, AYA-
419 ESP 2010-19082, AYA2011-29489-C03-01, AYA2012-39115-C03-01 and CSD2009-
420 00064 (Consolider MULTIDARK) and Comunidad de Madrid under project S2009/
421 ESP-1496. CALIPSO data used in the present work were obtained from the NASA
422 Langley Research Center Atmospheric Science Data Center. The authors wish to
423 thank anonymous reviewers for valuable comments to improve the manuscript.

424

References

- 425 1. Santangelo, A.; Picozza, P.; Ebisuzaki, T. et al. (JEM-EUSO Collaboration), “Status of the JEM-EUSO
426 Mission”, Proceedings of 33rd International Cosmic Ray Conference, Rio de Janeiro, ID0738 (2013).
- 427 2. Adams, J.H. Jr. ; Ahmad, S.; Albert, J.-N. et al. (JEM-EUSO Collaboration), “The JEM-EUSO mission
428 (An introduction to the focused issue)”, in this issue.
- 429 3. Takahashi, Y. and the JEM-EUSO Collaboration, “The JEM-EUSO Mission”, New Journal of Physics
430 11, 065009/1-21 (2009).
- 431 4. F. Kajino; Casolino, M.; Ebisuzaki, T. et al. (JEM-EUSO Collaboration), “The JEM-EUSO Instru-
432 ments”, Proceedings of 33rd International Cosmic Ray Conference, Rio de Janeiro, ID1128 (2013).
- 433 5. Adams, J.H. Jr.; Ahmad, S.; Albert, J.-N. et al. (JEM-EUSO Collaboration), “An overview of the JEM-
434 EUSO instrument”, in this issue.
- 435 6. For review, Letessier-Selvon, A.; Stanev, T., “Ultrahigh energy cosmic rays”, Review of Modern
436 Physics 83, 907–942 (2011).
- 437 7. Neronov, A.; Rodriguez Frías, M.D.; Toscano, S. et al. (JEM-EUSO Collaboration), “Atmospheric
438 Monitoring system of the JEM-EUSO telescope”, Proceedings of 33rd International Cosmic Ray Con-
439 ference, Rio de Janeiro, ID1072 (2013).
- 440 8. Adams, J.H. Jr.; Ahmad, S.; Albert, J.-N. et al. (JEM-EUSO Collaboration), “The AM system of the
441 JEM-EUSO instrument”, in this volume.
- 442 9. NASA, “ISS User’s Guide-Release 2.0” (2000).
- 443 10. JAXA Human Space Systems and Utilization Program Group, “Kibo Handbook” (2007).
- 444 11. Adams, J.H. Jr. ; Ahmad, S.; Albert, J.-N. et al., “An evaluation of the exposure in nadir observation
445 of the JEM-EUSO mission”, Astroparticle Physics 44, 76–90 (2013).
- 446 12. Adams, J.H. Jr. ; Ahmad, S.; Albert, J.-N. et al. (JEM-EUSO Collaboration), “The Photodetector
447 Module of the JEM-EUSO mission”, in this issue.
- 448 13. Catalano, O.; Bertaina, M.; Casolino, M. et al. (the JEM-EUSO Collaboration), “The trigger system of
449 JEM-EUSO Telescope” Proceedings of 31st International Cosmic Ray Conference, Lodz, #0326 (2009).
- 450 14. Rodriguez Frias, M.D.; Licandro, J.; Sabau, M.D. et al. (JEM-EUSO Collaboration), “Towards the
451 Preliminary Design Review of the Infra Camera of the JEM-EUSO Space Mission”, Proceedings of
452 33rd International Cosmic Ray Conference, Rio de Janeiro, ID0900 (2013).
- 453 15. Adams, J.H. Jr. ; Ahmad, S.; Albert, J.-N. et al. (JEM-EUSO Collaboration), “The Infrared Camera
454 onboard JEM-EUSO”, in this issue.
- 455 16. Toscano, S.; Valore, F.; Neronov, A. et al. (JEM-EUSO Collaboration), “An End to End Simulation
456 code for the IR-Camera of the JEM-EUSO Space Observatory”, Proceedings of 33rd International Cos-
457 mic Ray Conference, Rio de Janeiro, ID0514 (2013).
- 458 17. Toscano, S.; Valore, F.; Neronov, A. et al. (JEM-EUSO Collaboration), “LIDAR treatment inside the
459 ESAF Simulation Framework for the JEM-EUSO mission”, Proceedings of 33rd International Cosmic
460 Ray Conference, Rio de Janeiro, ID0530 (2013).
- 461 18. Mernik, T.; Guzman, A.; Fenu, F. et al. (JEM-EUSO Collaboration), “Simulating the JEM-EUSO
462 Mission: Expected Reconstruction Performance”, Proceedings of 33rd International Cosmic Ray Con-
463 ference, Rio de Janeiro, ID1072 (2013).
- 464 19. Adams, J.H. Jr. ; Ahmad, S.; Albert, J.-N. et al. (JEM-EUSO Collaboration), “Performances of JEM-
465 EUSO: energy and X_{\max} reconstruction”, in this issue.;
- 466 20. Adams, J.H. Jr. ; Ahmad, S.; Albert, J.-N. et al. (JEM-EUSO Collaboration), “Performances of JEM-
467 EUSO: angular reconstruction”, in this issue.
- 468 21. Berat, C.; Bottai, S.; De Marco, D. et al., “ESAF: Full Simulation of Space-Based Extensive Air
469 Showers Detectors”, Astroparticle Physics 33, 211–247 (2010).
- 470 22. Deirmendjian, D., “Electromagnetic Scattering on Spherical Polydispersions”, American Elsevier
471 Publishing Company Inc., New York (1969).
- 472 23. Liou, K.N., “Radiation and Cloud Processes in the Atmosphere”, Oxford University Press (1992).
- 473 24. CALIPSO, http://www.nasa.gov/mission_pages/calipso/main/
- 474 25. TOVS, <http://www.ozonlayer.noaa.gov/action/tovs.htm/>
- 475 26. A-Train Constellation, <http://http://atrain.nasa.gov/>
- 476 27. CALIOP, <http://www-calipso.larc.nasa.gov/about/payload.php#CALIOP>
- 477 28. Garnier, A; Pelon, J.; Dubuisson, P. et al., “Retrieval of Cloud Properties Using CALIPSO Imaging
478 Infrared Radiometer. Part I: Effective Emissivity and Optical Depth”, Journal of Applied Meteorology
479 and Climatology 51, 1407–1425 (2012).
- 480 29. Garino, F., Master Thesis, University of Torino (2011) and references therein.
- 481

-
- 482 30. Eg. Peel, M.C.; Finlayson, B.L. and McMahon, T.A., “Updated world map of the Köppen-Geiger
483 climate classification”, *Hydrology and Earth System Sciences* 11, 1633–1644 (2007).
- 484 31. Adams, J.H. Jr.; Ahmad, S.; Albert, J.-N. et al. (JEM-EUSO Collaboration), “The JEM-EUSO obser-
485 vational technique and exposure”, in this issue.
- 486 32. Roh, S.; Kim, J; Ryu, D. et al., “A comparison study of CORSIKA and COSMOS simulations for
487 extensive air showers”, *Astroparticle Physics* 44, 1–8 (2013).
- 488 33. Abu-Zayyad, T.; Jui, C.C.H. and Loh, E.C., “The effect of clouds on air showers observation from
489 space”, *Astroparticle Physics* 21, 163–182 (2004).